STATISTICAL SHAPE ANALYSIS OF BRAIN ARTERIAL NETWORKS (BAN)

By Xiaoyang Guo¹, Aditi Basu Bal¹ and Tom Needham² Anuj Srivastava¹

¹Department of Statistics, Florida State University, xiaoyang.guo.fl@gmail.com; ab18z@my.fsu.edu; anuj@stat.fsu.edu

²Department of Mathematics, Florida State University, tneedham@fsu.edu

Structures of arterial networks in the human brain, termed Brain Arterial Networks or BANs - that are complex arrangements of individual arteries, their branching patterns, and inter-connectivities - play an essential role in characterizing and understanding brain physiology. One would like tools for statistically analyzing the shapes of BANs, i.e., quantifying shape differences, comparing a population of subjects, and studying the effects of covariates on these shapes. This paper mathematically represents and statistically analyzes BAN shapes as elastic shape graphs. Each elastic shape graph consists of nodes, or points in 3D, connected by some 3D curves, or edges, with arbitrary shapes. We develop a mathematical representation, a Riemannian metric and other geometrical tools, such as computations of geodesics, means, covariances, and PCA, for helping analyze BANs as elastic graphs. We apply this analysis to BANs after dividing them into four components – top, bottom, left, and right. The framework is then used to generate shape summaries of BANs from 92 subjects and study the effects of age and gender on shapes of BAN components. We conclude that while gender effects require further investigation, age has a clear, quantifiable effect on BAN shapes. Specifically, we find an increased variance in BAN shapes as age increases.

1. Introduction. The human brain is one of the most sophisticated organs in the human body and serves as the center of the nervous system. It requires a significant amount of energy to accomplish its designated tasks and a complex network of arteries is used to supply the necessary oxygen and nutrition to parts of the brain. This network, called the *Brain arterial network* or BAN, is central to maintaining standard anatomical functionality of the brain. The structure or morphology of BANs determines their effectiveness in providing supply lines and in characterizing and diagnosing brain health. Consequently, a statistical analysis of BANs, which constitutes representing and analyzing shape variability within and across human populations is a significant problem area. However, this analysis is challenging because the BANs have complicated structures, with tremendous variability in terms of branching, winding, and merging nature of arteries on the one hand, and the shapes and sizes of arteries on the other.

Fig. 1 shows some examples of BANs for different human subjects. Each BAN is reconstructed from a 3D Magnetic Resonance Angiography (MRA) image using a tube-tracking vessel segmentation algorithm [Aydın et al. (2009); Aylward and Bullitt (2002)]. Given the complex nature of BANs, previous analyses have primarily focused on first extracting some low-dimensional features from the original data, followed by a statistical analysis of these features. One of the earliest analyses [Bullitt et al. (2010)] focused on some simple geometrical summaries, such as the numbers and the lengths of the arteries. In recent years, the extracted features have become more sophisticated. For instance, Bendich et al. (2016) uses tools from Topological Data Analysis (TDA), where one extracts certain mathematical features (e.g., persistent homology) from the data and compares these features using certain metrics [Wasserman (2018)]. However, the difficulty in such feature-based approaches is that

these representations are typically not invertible. Feature extraction usually represents only partial information about the original objects, forming a many-to-one mapping (from the object space to a feature space). Moreover, it is not clear as to which set of shapes share the same topological features. Because of this lack of invertibility, it is not easy to map solutions or statistical inferences back to the object space. This paper takes a more ambitious approach, where we develop a statistical analysis of BANs in the original space itself without resorting to extracting any features. In the process, we seek solutions – shape summaries, shape PCA, and shape models – that can be studied as BANs themselves.

Besides BANs, there are other biological and anatomical objects with similar shape architectures, displaying complex filamentary shapes. Examples include retinal blood vessels [Hoover, Kouznetsova and Goldbaum (2000)], vein structures in fruit fly wings [Sonnenschein et al. (2015)] and neurons [Kong et al. (2005)]. A defining characteristic of these objects is that they are composed of a network of 2D/3D curves, each with arbitrary shapes and sizes. Moreover, these curves merge and branch at arbitrary junctions and result in intricate patterns of pathways. While we mainly focus on BANs in this paper, the proposed framework is also applicable to these other application domains. Statistical shape analysis of such objects is difficult because, to quantify shape differences, one needs to consider the numbers, locations, branchings, and shapes of individual curves. In particular, one has to solve a difficult problem of *registration of points and parts* across objects, *i.e.*, which points on a branch on one object matches with which points or parts on the other.

The field of shape analysis has steadily gained relevance and activity over the last two decades. This rise is fueled by the availability of multimodal, high-dimensional data that records objects of interest in various contexts and applications. Shapes of objects help characterize their identity, classes, movements, and roles in larger scenes. Consequently, many approaches have been developed for comparing, summarizing, modeling, testing, and tracking shapes in a static image or video data. Statistical shape analysis requires mathematical representations and proper metrics. While early methods generally relied on discrete representations of shapes [Kendall (1984); Kendall et al. (1999); Small (1996); Dryden and Mardia (2016)], more recent methods have focused on continuous objects such as scalar functions [Srivastava and Klassen (2016)], Euclidean curves [Younes (1998); Klassen et al. (2004); Younes et al. (2008); Srivastava and Klassen (2016)], and 3D surfaces [Jermyn et al. (2017)]. The main motivation for this paradigm shift comes from the need to address the registration problem, considered the most challenging issue in shape analysis. As mentioned earlier, registration refers to establishing a correspondence between points or features across objects and is an important ingredient in comparing shapes. Continuous representations of objects use actions of the re-parameterization groups to help solve dense registration problems. Furthermore, they use elastic Riemannian metrics – which are invariant to the actions of re-parameterization groups – and some simplifying square-root representations to develop very efficient techniques for comparing and analyzing shapes.

While elastic Riemannian shape analysis is considered well developed for elementary objects – Euclidean curves [Younes et al. (2008); Srivastava et al. (2011)], manifold-valued curves [Zhang, Klassen and Srivastava (2018); LeBrigant (2019)], 3D surfaces [Jermyn et al. (2012)], trees [Duncan et al. (2018); Wang et al. (2020)] - the problem of analyzing more complex objects remains less explored. In other words, the past work has mainly focused on objects that exhibit only the geometrical variabilities while being of the same or similar topologies. Similar topologies help pose the registration problem as that of optimal (diffeomorphic) re-parameterization of the common domain. In this paper, we are concerned with comparing BANs that can potentially differ in both topologies and geometries.

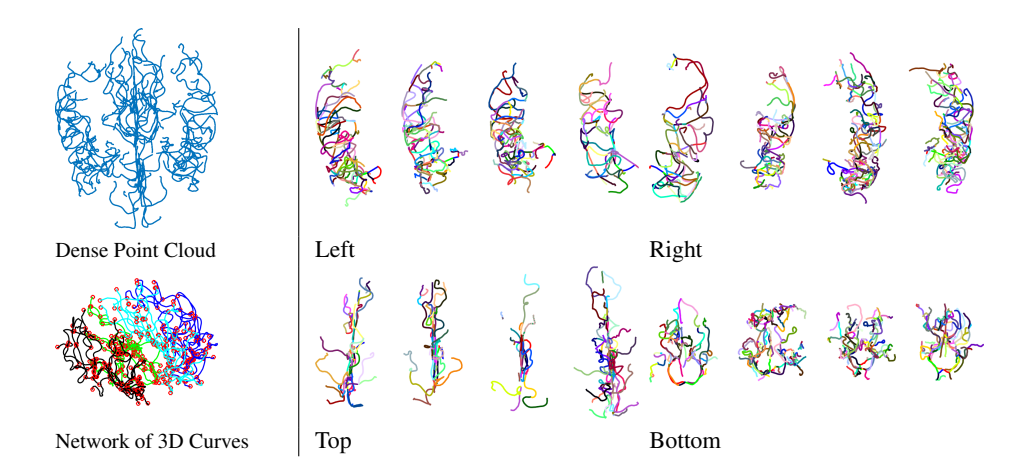


FIG 1. Examples of brain arterial networks. Left side is the different representations of BAN data. Cyan, black, green, and blue display the four components: top, left, bottom, and right, respectively. Red circles denote nodes. Right side is examples of four components of BANs from different subjects.

Specific Goals: Our goal here is to develop a suite of techniques for statistical analysis of BAN shapes. Specifically, we seek: (1) a **shape metric** that is invariant to the usual shape-preserving transformations, (2) elastic **registration** of parts across BANs, (3) computation of **geodesic** paths between any two BANs and (4) computation of **statistical summaries** – mean, covariance, PCA – in the shape space of BANs. These tools, in turn, can be used for analysis, clustering, classification, and modeling of shapes in conjunction with other machine learning methods. We reiterate that existing techniques may provide some but not all of these solutions.

Our approach is to view BANs as extensions of traditional graphs with the usual node-edge representations. The difference lies in that edge characterization is now more sophisticated each edge is a full shape of a curve connecting the corresponding nodes, as shown on the right side of Fig. 1. These graphs, called *elastic graphs*, are represented by their adjacency matrices, with matrix elements given by the shapes of the corresponding edges. Since the ordering of nodes in these graphs and the subsequent indexing of adjacency matrices is arbitrary we model this variability using the action of the permutation group and represent each shape as an orbit under this group. Then, we develop techniques for optimization under this permutation group (also known as *graph matching*), leading to computations of geodesics and summaries under the induced metric on the Riemannian quotient space, termed the *graph shape space*. There is no current geometrical framework for the shape analysis of such graphical objects. While TDA and other such methods can measure dissimilarity in shapes, this paper provides more comprehensive statistical quantities, such as mean, covariance, and principal components, for a more in-depth shape summarization and modeling.

In order to further tame the complexity and to improve registration results, we divide a BAN into four components – top, bottom, left, and right – as shown in different colors on the left side of Fig. 1. This division is not always precise, but the subsequent statistical analysis is generally robust to small variations in the division. Then, we study each of these components independently, as separate objects. Right side of Fig. 1 shows some examples of these four components from different subjects.

2. Proposed Mathematical Framework. We now present a mathematical framework for representing elastic graphs, keeping in mind that BAN components form the focus of this study. The proposed framework can be viewed as an extension of some previous works

on graphs [Calissano, Feragen and Vantini (2020); Chowdhury and Needham (2020); Guo, Srivastava and Sarkar (2021); Jain and Obermayer (2009, 2011, 2012)]. However, those past works are restricted to only scalar-weighted graphs and do not consider more sophisticated features such as edge shapes.

2.1. Elastic Graph Representation. We are interested in objects made of several 3D curves, with arbitrary shapes and placements, that merge and branch at arbitrary junctions and result in networks of pathways. We will represent them as graphs with nodes corresponding to junctions and edges corresponding to the shapes of 3D curves connecting the nodes. Here we assume that any two nodes are connected directly by at most one curve. An edge attributed graph G is an ordered pair (V,a), where V is a set of nodes and a is an edge attribute function: $a:V\times V\to \mathcal{S}$. \mathcal{S} is the shape space of elastic 3D curves that is briefly discussed next.

The edges in elastic graphs are Euclidean curves and to analyze their shapes we use elastic shape analysis framework described in [Srivastava and Klassen (2016)]. Let $\beta:[0,1]\to$ \mathbb{R}^n , n=2 or 3, be an absolutely continuous function, representing a parametrized curve. Define the square root velocity function (SRVF) of β as: $q(t) = \frac{\dot{\beta}(t)}{\sqrt{|\dot{\beta}(t)|}} \in \mathbb{R}^n$, if $|\dot{\beta}(t)| \neq 0$ and zero otherwise. One can recover β from its SRVF using $\beta(t) = \beta(0) + \int_0^t q(s)|q(s)|ds$. If β is absolutely continuous, the SRVF is square-integrable, i.e., $q \in \mathbb{L}^2([0,1],\mathbb{R}^n)$ or simply \mathbb{L}^2 . It can be shown that the \mathbb{L}^2 norm on SRVF space is an elastic Riemannian metric on the original curve space. Therefore, one can compute the elastic (i.e., rotation and reparameterizationinvariant) distance between two curves β_1, β_2 using $d(\beta_1, \beta_2) = ||q_1 - q_2||_{\mathbb{L}^2}$. One of the most important challenges in shape analysis is registration, a dense correspondences across curves. Let $\gamma:[0,1]\to[0,1]$ be a diffeomorphism; in classical elastic shape analysis, diffeomorphisms are restricted to be orientation-preserving ($\gamma(0) = 0$ and $\gamma(1) = 1$), but in the proposed framework we make no such restriction. The action of the diffeomorphism group on an SRVF q is $q * \gamma = (q \circ \gamma)\sqrt{\gamma}$. This is same the expression as the SRVF of the re-parameterized curve: $\beta \circ \gamma$. To register points across curves, one mods out this re-parametrization group as follows. Each shape can be represented by orbits under the re-parametrization group: $[q] = \{q * \gamma | \gamma \in \Gamma\}$. The set of all orbits is the shape space of curves in \mathbb{R}^n is denoted $\mathcal{S} = \{[q] | q \in \mathbb{L}^2\}$. The shape metric is then given by: $d_s([q_1], [q_2]) = \inf_{\gamma} ||q_1 - (q_2 * \gamma)||$. By including both orientation-preserving and reversing diffeomorphisms, the shape distance between a curve $(\beta(t))$ and its parameterized reflection $(\beta(1-t))$ is zero.

One can use this metric d_s to define and compute averages of shapes of curves and their PCA analysis. For further details, we refer the reader to the textbook [Srivastava and Klassen (2016)].

REMARK 1. Note that traditionally one further removes the rotation and scale of curves from considerations in shape analysis, but here these two variables are integral to the shapes of arteries and the network as a whole. So, we do not remove them. We do perform a global scale and rotational alignment of the whole BAN when comparing it with another BAN.

Returning to the elastic graph, the shape $a(v_i,v_j)=[q_{ij}]$ characterizes the shape of curve connecting the nodes $v_i,v_j\in V, i\neq j$. Since the representation $[q_{ij}]$ includes both a curve and its parameterized reflection, this edge attribute is directionless. Assuming that the number of nodes is n,G can be represented by its adjacency matrix $A=\{a_{ij}\}\in\mathcal{S}^{n\times n}$, where the element $a_{ij}=a(v_i,v_j)$. For an undirected graph G, we have $a(v_i,v_j)=a(v_j,v_i)$ and therefore A is a symmetric matrix. As an example, the adjacency matrix of the third graph shown in

Fig. 2 is given by

$$\begin{pmatrix} \mathbf{0} & [q_{12}] & \mathbf{0} & \cdots & [q_{18}] \\ [q_{21}] & \mathbf{0} & [q_{23}] & \cdots & [q_{28}] \\ \mathbf{0} & [q_{32}] & \mathbf{0} & \cdots & \mathbf{0} \\ \vdots & \vdots & \vdots & \ddots & \vdots \\ [q_{81}] & [q_{82}] & \mathbf{0} & \cdots & \mathbf{0} \end{pmatrix} \in \mathcal{S}^{n \times n},$$

where $\mathbf{0}$ denotes a null edge. It implies that the corresponding nodes are not connected and we substitute the constant zero function $\mathbf{0} \in \mathbb{L}^2$ as its shape. Note that $[\mathbf{0}] = \mathbf{0}$ is an element of the shape space \mathcal{S} and one can perform all the standard operations, such as computing shape distance, computing averages, or performing tangent PCA, with null edges using the geometry of \mathcal{S} . A little later we will also use the concept of null nodes, extraneous nodes that are attached to the existing graphs using null edges. This use of null nodes facilitates improved matching and comparisons of graphs. As mentioned earlier, we will assume that there are no self-loops in BANs and therefore the diagonal entries in A will also be null. The set of all such adjacency matrices is given by $\mathcal{A} = \{A \in \mathcal{S}^{n \times n} | A = A^T, \operatorname{diag}(A) = \mathbf{0}\}$.

In some situations, it may be useful to include the node attributes also in graph comparisons. In this paper, we use the degree of a node, *i.e.*, the number of other nodes connected to a node by non-trivial edges, as its attribute. Let $u \in \mathbb{R}^n$ denote the vector of node attributes associated with the graph. Note that the ordering of nodes in u matches the ordering of nodes in A. Combining the node-edge representations we get a joint representation $B = (A, u) \in \mathcal{A} \times \mathbb{R}^n \equiv \mathcal{B}$.

Next we define a metric for comparing graphs. We will start by assuming that all the graphs have the same number of nodes, but will include graphs with arbitrary number of nodes shortly. For any two $A_1, A_2 \in \mathcal{A}$, with the corresponding entries a_{ij}^1 and a_{ij}^2 , respectively, we define the edge metric d_a to be: $d_a(A_1,A_2) \equiv \sqrt{\sum_{i,j} d_s(a_{ij}^1,a_{ij}^2)^2}$. d_a quantifies the differences between adjacencies of graphs, A_1 and A_2 , where d_s is the shape metric for curves as defined above. Additionally, let the matrix of distances between the node attributes u_1, u_2 to be: $D = |u_1 \mathbf{1}_n^T - \mathbf{1}_n u_2^T|$, where $\mathbf{1}_n$ is an n-vector of all ones. Thus, D_{ij} is difference between the attributes of nodes v_i^1 and v_j^2 . This leads to a node metric between two graphs according to $d_v = \text{Tr}(D)$. Finally, we can combine the two metrics to reach a composite metric: $d_b(B_1, B_2) \equiv d_a + \lambda \operatorname{Tr} D$, where λ is the relative weight between the contributions of the edges and the nodes.

Under the chosen metric, the geodesic or the shortest path between two points in \mathcal{A} can be written as a set of geodesics in \mathcal{S} between the corresponding components. That is, for any $A_1, A_2 \in \mathcal{A}$, the geodesic $\alpha: [0,1] \to \mathcal{A}$ consists of components $\alpha = \{\alpha_{ij}\}$ given by $\alpha_{ij}: [0,1] \to \mathcal{S}$, a uniform-speed geodesic path in \mathcal{S} between a^1_{ij} and a^2_{ij} . Note that this solution also provides an optimal registration of points across edges a^1_{ij} and a^2_{ij} . Also, if needed, one can linearly interpolate between the attributes of the corresponding nodes, to provide node attributes for the intermediate graphs.

The main issue in this comparison is that the indexing of nodes in the graphs A_1 and A_2 is arbitrary and, thus, corresponding matching of edges a_{ij}^1 with a_{ij}^2 is also arbitrary. To illustrate this point, Fig. 2 shows the same graphical object several times and imposes a different node indexing every time. In order to provide a reasonable comparison of these graphs using the metric d_a , one has to reorder nodes every time we compare any two graphs. Otherwise, we will end up with large d_a distances between these graphs despite having the same structure. We shall use the permutation group to implement this reordering. This permutation is similar to the work by Jain and Obermayer (2009, 2011) on graphs with Euclidean attributes. A permutation matrix is a matrix that has exactly one 1 in each row and column, with all the other entries being zero. Let \mathcal{P} be the group of all $n \times n$ permutation matrices with group

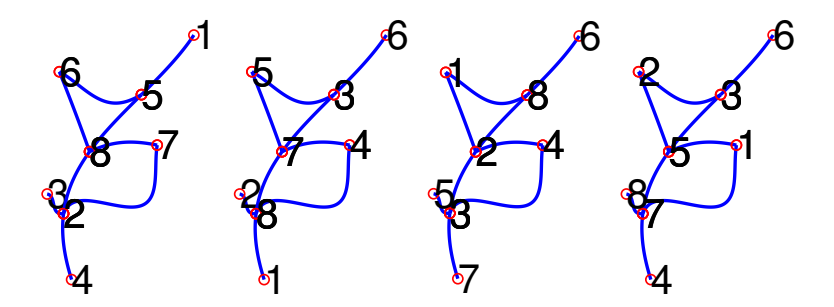


FIG 2. Four graphs with the same shape but with different node labels.

operation being matrix multiplication and identity element being the $n \times n$ identity matrix. We define the action of \mathcal{P} on \mathcal{B} as:

(2.1)
$$\mathcal{P} \times \mathcal{B} \to \mathcal{B}, P \star (A, u) = (P \cdot A \cdot P^T, Pu).$$

Since each entry of A is an element of the shape space S, this group action denotes a permutations of *shapes* in that matrix. Here \cdot implies a permutation of entries of A according to the nonzero elements of P. The action $P \star A$ results in the swapping of rows and columns of A. The elements of the node attribute vector u are permuted according to P in the same way. Under the chosen metric $d_b = d_a + \lambda \operatorname{Tr}(D)$, this mapping is isometric.

- LEMMA 1. 1. **Permutation Group**: The action of \mathcal{P} on the set \mathcal{B} given in Eqn. 2.1 is by isometries. That is, for any $P \in \mathcal{P}$, $A_1, A_2 \in \mathcal{A}$ and $u_1, u_2 \in \mathbb{R}^n$, we have $d_b((A_1, u_1), (A_2, u_2)) = d_b(P \star (A_1, u_1), P \star (A_2, u_2))$.
- 2. **Global Rotation Group**: The action of the rotation group SO(d), d=2,3 on \mathcal{B} , is given by $(A,u)\mapsto (O\odot A,u)$, which implies that each element of A is rotated by the same O. In other words, $(O\odot A)_{ij}=Oa_{ij}$, for all i,j. Note that the node attributes here are assumed to be invariant to graph rotations. This rotation action on \mathcal{B} is also by isometries. That is, for any $O\in SO(d)$ and $(A_1,u_1),(A_2,u_2)\in \mathcal{B}$, we have $d_b((A_1,u_1),(A_2,u_2))=d_b(O\odot (A_1,u_1),O\odot (A_2,u_2))$.

Under the joint action of \mathcal{P} and SO(d), the orbit of an $(A,u) \in \mathcal{B}$ is given by: $[(A,u)] = \{O \odot (P \star (A,u)) | P \in \mathcal{P}, O \in SO(d)\}$. Any two elements of an orbit denote the same graph shape, except that the nodes' ordering has changed and the graph is rotated. Orbit membership defines an equivalence relation \sim on \mathcal{A} : $(A_1,u_1), (A_2,u_2) \in [A_1]$ implies

$$(A_1, u_1) \sim (A_2, u_2) \Leftrightarrow \exists P \in \mathcal{P}, O \in SO(d) : O \odot (P \star (A_1, u_1)) = (A_2, u_2)$$
.

The set of all equivalence classes forms the quotient space: $\mathcal{G} \equiv \mathcal{B}/(\mathcal{P} \times SO(d)) = \{[(A,u)]|(A,u) \in \mathcal{B}\}$. Henceforth, we will call \mathcal{G} the *elastic graph shape space*.

LEMMA 2. Since the finite-dimensional group $\mathcal{P} \times SO(d)$ acts by isometries under the metric $d_b = d_a + \lambda d_v$, there is a well-defined induced metric on the quotient space \mathcal{G} , defined by

(2.2)
$$d_g([(A_1, u_1)], [(A_2, u_2)]) = \min_{P \in \mathcal{P}, O \in SO(d)} d_b((A_1, u_1), O \odot (P \star (A_2, u_2))).$$

Since the Lie group $\mathcal{P} \times SO(d)$ is compact, the minimum in (2.2) exists. Note that the solution may not be unique, *i.e.*, their may be multiple ways to register two graphs optimally. If

$$(\hat{P}, \hat{O}) \in \underset{P \in \mathcal{P}, O \in SO(d)}{\operatorname{argmin}} d_b((A_1, u_1), O \odot (P \star (A_2, u_2))),$$

then (A_1,u_1) and $\hat{O}\odot(\hat{P}\star(A_2,u_2))$ are considered to be *aligned and registered*. The shortest path between $[(A_1,u_1)]$ and $[(A_2,u_2)]$ under the metric d_g is given by $[\alpha(t)]$ where $\alpha:[0,1]\to\mathcal{B}$ is: (1) for edges a geodesic between A_1 and $\hat{O}\odot(\hat{P}\star A_2)$ and (2) for nodes it is a straight line between u_1 and $\hat{P}u_2$. This shortest path is a geodesic in the sense that each of its component is a geodesic in \mathcal{S} between the registered edges.

2.2. Graph Matching. The problem of optimization over \mathcal{P} , stated in Eqn. 2.2, is an instance of a generalized graph matching problem and is the most important challenge in the proposed framework. Given an optimal $P \in \mathcal{P}$, the optimization over SO(d) is straightforward, and the result is obtained using the Procrustes method. We will not discuss it further and will focus only on graph matching. This matching problem is, in fact, NP complete [Yan et al. (2016)], and its global solution cannot be found in a reasonable time as the graph size increases. Instead, one uses relaxation techniques to find approximate solutions in one of several ways.

If the adjacency matrix A were real-valued and edge similarities were measured by the Euclidean norm, then the matching problem can be written as $\hat{P} = \arg\min_{P \in \mathcal{P}} \|A_1 - PA_2P^T\| = \arg\max_{P \in \mathcal{P}} \operatorname{Tr}(A_1PA_2P^T)$. This particular formulation is known as *Koopmans-Beckmann's* quadratic assignment programming (QAP) problem [Koopmans and Beckmann (1957)]. In this case, one can use an existing relaxation solution for approximating the optimal registration [Caelli and Kosinov (2004); Liu, Qiao and Xu (2012); Umeyama (1988); Vogelstein et al. (2015)].

However, when elements of \mathcal{A} belong to a more general metric space, e.g., shape space \mathcal{S} , some of the previous solutions are not applicable. Instead, the problem can be rephrased as $\hat{P} = \arg\max_{P \in \mathcal{P}} \operatorname{vec}(P)^T K \operatorname{vec}(P)$, where $\operatorname{vec}(P)$ denotes a concatenation of elements of P in a column vector. Here $K \in \mathbb{R}^{n^2 \times n^2}$, called an *affinity matrix*, has the following structure. Suppose A_1 has node index a, b, etc. and A_2 has node index i, j, etc. Then,

- the diagonal entries k_{aiai} measure the affinity between node a of A_1 and node i of A_2 , and
- the off-diagonal entries k_{aibj} measures the affinity between edge ab of A_1 and edge ij of A_2 .

In this paper we use the shape similarity between two edges, while modding out the reparametrization group, as affinity:

$$k_{aibj} = \begin{cases} 0, \text{ if either } a_{ab}^1 \text{ or } a_{ij}^2 \text{ is null} \\ \sup_{\gamma} \langle q_1, O(q_2 \circ \gamma) \sqrt{\dot{\gamma}} \rangle, \text{ otherwise} \end{cases}.$$

Note that this sup over γ is related to the infimum over γ in the definition of d_s because:

$$||q_1 - O(q_2 * \gamma)||^2 = ||q_1||^2 + ||q_2||^2 - \langle q_1, O(q_2 \circ \gamma) \sqrt{\dot{\gamma}} \rangle$$
.

Here q_1,q_2 denote the SRVFs of the edges ab of A_1 and ij of A_2 and γ is a diffeomorphic reparameterization and the supremum, computed using the Dynamic Programming Algorithm (DPA) [Srivastava et al. (2011)]. The matrix $O \in SO(d)$ is the global rotation matrix that is used to rotationally align two elastic graphs. (The same O matrix is applied to all the edges of the second graph and minimized using the Procrustes rotation.) When $\lambda > 0$ and node attributes are involved in shape analysis, we can set $k_{aiai} = \lambda \exp(-\frac{|u_1(a) - u_2(i)|^2}{2\sigma^2})$. In practice, the choice of λ and σ are an issue and one can use learning or cross-validation to estimate suitable values.

The resulting formulation is called the *Lawler's QAP problem* [Lawler (1963)]. Koopmans-Beckmann's QAP is a particular case of Lawler's QAP. To solve for Lawler's QAP, at least approximately, there are several algorithms available [Cour, Srinivasan and Shi (2007); Gold

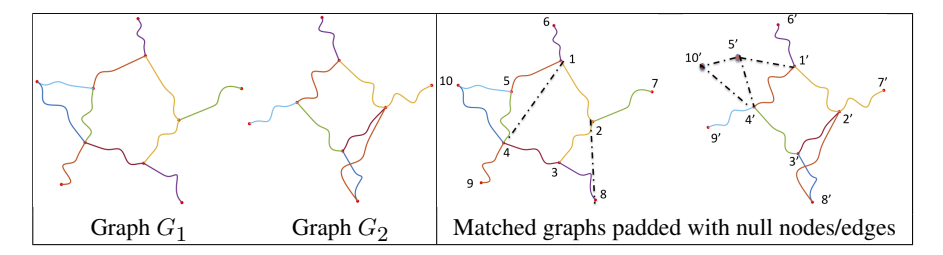


FIG 3. Labeling and addition of null nodes in order to facilitate registration between two graphs.

and Rangarajan (1996); Leordeanu and Hebert (2005); Leordeanu, Hebert and Sukthankar (2009); Zanfir and Sminchisescu (2018); Zhou and De la Torre (2012, 2015)]. In this paper, we use the well-known factorized graph matching (FGM) algorithm [Zhou and De la Torre (2015)] to match elastic graphs. As mentioned previously, we need to optimize edge affinity over both orientation-preserving and reversing diffeomorphisms, to allow for the possibility of an orientation-reserving registration (the original DPA is only applicable for orientation-preserving diffeomorphisms). We can work around it using the directed FGM. We treat each edge a_{ij} in the graph as two directed edges: one from i to j and one from j to i. The edge affinity between any two edges is evaluated four times (two directions of one edge times two directions of another edge) using the original DPA. In practice, we calculate the affinities only twice and use each value twice.

2.3. Introducing Null Nodes. Thus far, we have assumed that the graphs being matched are all of the same size (in terms of the number of nodes). For graphs G_1 and G_2 , with different numbers of nodes n_1 and n_2 , we can append them with n_2 and n_1 null nodes, respectively, to bring them each to the same size $n_1 + n_2$. This addition of null nodes can be done even when they are the same size, as it can help improve graph matching. This way, the original (real) nodes of both G_1 and G_2 can potentially be registered to null nodes in the other graph and bring down the matching cost.

When we add null nodes to a graph, we need to assign attributes to these extra nodes and edges thus created. We set the edges connected to null nodes to have a value $\mathbf{0} \in \mathcal{S}$. In other words, we extend the adjacency matrices of the two graphs from A_i to \tilde{A}_i as shown below. For the null nodes, we do not assign the node attributes explicitly. Instead, we extend the node distance matrix D to \tilde{D} by setting the entries corresponding to the null nodes to be zero. This setting implies that the null nodes' attributes are equal to those of the nodes they are being matched to in the other graph. This choice ensures that the attributes of null nodes do not contribute to the matching cost. The extended matrices are constructed as follows:

$$\tilde{A}_{1} = n_{2} \left\{ \begin{array}{ccc} \overbrace{A_{1} & \mathbf{0}} \\ \mathbf{0} & \mathbf{0} \end{array} \right] \quad \begin{array}{ccc} n_{2} & \overbrace{A_{2} & \mathbf{0}} \\ A_{2} = n_{1} \left\{ \begin{array}{ccc} \overbrace{A_{2} & \mathbf{0}} \\ \mathbf{0} & \mathbf{0} \end{array} \right] , \quad \tilde{D} = n_{2} \left\{ \begin{array}{ccc} \overbrace{D} & \mathbf{0} \\ \mathbf{0} & \mathbf{0} \end{array} \right].$$

Once we have extended the graphs using the null nodes, we apply the same matching procedure as before. In terms of displaying the extended graphs, we do not display null nodes matched with null nodes. The null nodes matched with real nodes are assigned the same coordinates, as their matched counterparts, for display purposes.

Figure 3 shows an example of this idea. The left side shows two graphs that have different number of nodes and edges, but still seem to have a common structure. On the right side we label the nodes to show a particular matching of these graphs. The matched nodes are

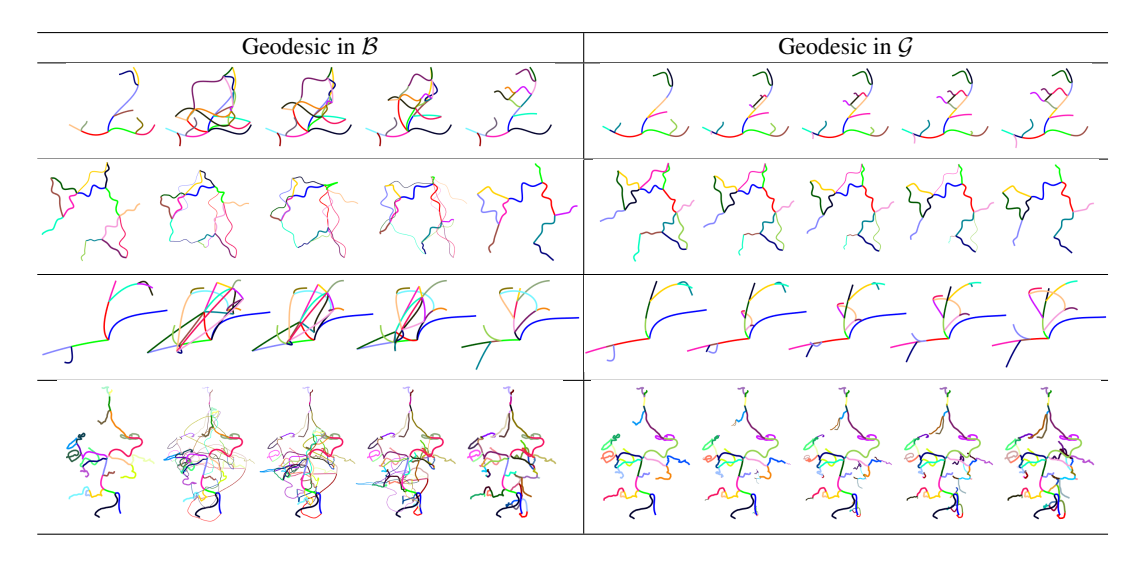


FIG 4. Geodesic between graphs in space \mathcal{B} (left) and the \mathcal{G} (right). Coloring is used to depict registration of edges across graphs. The top two rows show 2D graphs while bottom two use 3D graphs. (GIF animations of these geodesics are provided with the supplementary material [Guo et al. (2021)].)

labelled 1-1', 2-2', and so on. We obtain this matching by adding two null nodes: 5' and 10', and corresponding null edges $1' \leftrightarrow 5'$, $10' \leftrightarrow 5'$, $10' \leftrightarrow 4'$, $5' \leftrightarrow 4'$ in G_2 , and the null edges $1 \leftrightarrow 4$, $2 \leftrightarrow 8$ in G_1 . We emphasize that the matching between graphs is performed at the node level and is one-to-one. This framework does not allow nodes to split or merge when registering across graphs (as in, e.g., Chowdhury and Needham (2020)). Consequently, the edges (where real or null) are also matched in a one-to-one fashion. Once again, there is no split or merging of edges allowed when matching graphs. For instance, in Fig. 3, the edge $1 \leftrightarrow 4$ can only be matched with a single edge, say $1' \leftrightarrow 4'$, but can not be matched with the pair say $1' \leftrightarrow 5' \leftrightarrow 4'$.

Once we match the two graphs, we can compute geodesics between them by interpolating between the corresponding nodes and edges (according to their respective metrics). We present four illustrative examples in Fig. 4. The two graphs G_1 and G_2 drawn as the first and the last graphs in each picture in each sequence. Additionally, we show a sequence of shapes along the geodesic path between them in two different spaces – \mathcal{B} and \mathcal{G} , *i.e.*, with arbitrary registration and with optimal registration. The deformations between registered graphs, associated with geodesics in \mathcal{G} , look much more natural than those in \mathcal{B} . The edge features are preserved better in the intermediate graphs along the geodesics in \mathcal{G} . The edges in one graph that are unmatched in the other graph either disappear or appear along the geodesic. We can display this effect using either thickening/thinning or shrinking/growing of edges. For internal edges, the change in thickness seems more appropriate, but for the terminal edges, i.e., edges that have a node with only one edge attached to it, it seems more natural to shorten (lengthwise) a non-null edge into a null edge. Note that the framework currently does not utilize any information about edge thickness in shape comparisons. This property is manipulated only for display purposes. The top two rows are for 2D graphs, while the remaining examples are 3D graphs. As mentioned earlier, the points along registered edges of graphs are registered while computing d_s . Thus, we reach a dense (complete) registration of parts across the two graphs, making the deformations appear more natural.

3. Shape Summaries of Elastic Graphs. We are interested in tools that facilitate statistical inferences for the given BAN dataset. These inferences include classification, clustering, hypothesis testing, and modeling. The use of a metric structure to compute summaries

of shapes of graphs is of great importance in these analyses. We will use the earlier metric structure to define and compute shape statistics – such as mean, covariance, and PCA – of given graph data. Further, we will use these representations to perform dimension reduction and hypothesis testing.

3.1. Mean Graph Shapes. Given a set of graph shapes $\{[A_i] \in \mathcal{G}, i = 1, 2, ..., m\}$, we define their mean graph shape to be:

$$[A_{\mu}] = \underset{[A] \in \mathcal{G}}{\operatorname{arg \, min}} \left(\sum_{i=1}^{m} d_g([A], [A_i])^2 \right) ,$$

where d_g is as defined in Eqn. 2.2. This construction has been named Fréchet, Karcher, or intrinsic mean interchangeably. There are at least two different ways of computing this mean. One relies on the gradient of the cost function in this optimization, and the other relies on finding a sequence of geodesic paths. In the following, we focus on computing the means of the edge attributes, since the computation of node averages is relatively straightforward.

Method 1– Gradient Approach: Algorithm 1 outlines a gradient-based approach for computing the mean shape. This gradient solution is a local minimum of the cost functional and does not guarantee a global minimizer.

Algorithm 1 Graph Mean in \mathcal{G}

Given adjacency matrices A_i , i = 1, ..., m:

- 1: Initialize a mean template A_{μ} (e.g., the largest graph).
- 2: Rotationally align A_i s to A_μ using the Procrustes method.
- 3: Match A_i to A_μ under the permutation group $\mathcal P$ using FGM [Zhou and De la Torre (2015)] and SRVF [Srivastava and Klassen (2016)], store the matched graph shape as A_i^* , for i=1,...,m.
- 4: Update $A_{\mu} = \frac{1}{m} \sum_{i=1}^{m} A_{i}^{*}$. Since the graphs are all registered to A_{μ} , we can take a Euclidean average of the elements of A_{i}^{*} s here.
- 5: Repeat 2 and 3 until $\sum_{i=1}^m d_a(A_i^*,A_\mu)^2$ converges.

We present an example of computing mean graphs in Fig. 5. The top left side shows a set of 12 graphs whose mean is being computed. While these graphs have a common skeletal structure – a ringlike interior with radial offshoots – they also differ significantly in terms of the number of nodes/edges and shapes of edges. The mean of these graphs, computed using Algorithm 1, is shown in the figure's top right. It provides a reasonable visual and mathematical representation of the sample graphs, capturing the overall ringlike skeleton. The thickness of edges in the mean graph represents the frequency at which they appear in the given samples. One can always prune the thinner edges to improve clarity and focus on the larger, common structures.

Method 2 – Sequential Approach: This approach starts with any two graphs and computes their mean to initialize the current mean. It then sequentially compares the current mean and one additional individual graph at each time and computes their pairwise weighted mean. This weighted mean becomes the new current mean for the next step. The full algorithm is given below. The theoretical properties of this estimator of population mean are discussed in Chakraborty and Vemuri (2019).

The top right panel of Fig. 5 also shows the result of computing the mean shape using Algorithm 2. This shape denotes the mean of 12 graphs shown on the left side of this figure. Comparing this mean shape with the mean computed using Algorithm 1, we see a lot of

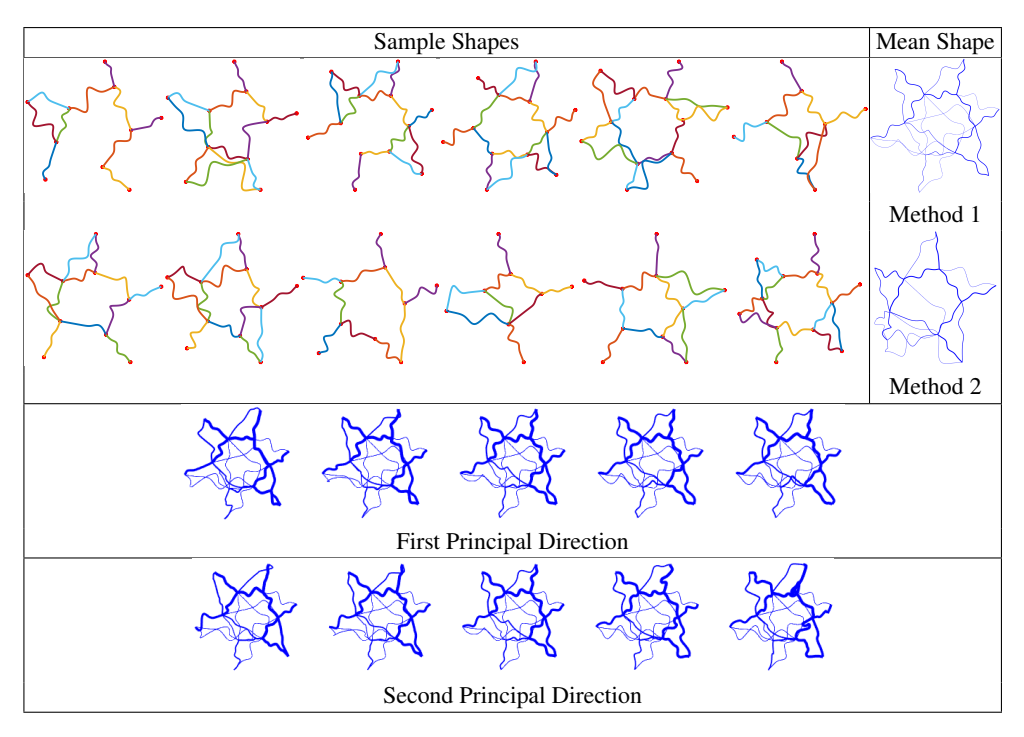


FIG 5. Mean and PCA of 12 sample graphs. The thickness of edges in the mean shape represents how often an edge is present in sample shapes. For PCA, in each row, the middle shape is the mean (method 1) while the right sides and left sides are perturbation from mean by $\pm 1, \pm 2$ square-root of the singular values.

Algorithm 2 Graph Mean in \mathcal{G}

Given adjacency matrices A_i , i = 1, ..., m:

- 1: Find the constant speed geodesic between A_1 and A_2 and set μ to be the halfway point.
- 2: For each $i=3,4,\ldots,m$, find the constant speed geodesic between μ and A_i . Set μ to the point at $\frac{1}{i}$ th distance from the previous μ along that new geodesic.

structural similarities, but we also see some visible differences in the shapes of individual edges across the two means. Ideally, these two results should be identical. We attribute these differences to several factors, including the numerical errors involved in different steps of these procedures, especially Algorithm 1. The differences can also result from each solution being a local rather than a global minimizer of the cost function.

3.2. Tangent PCA in Graph Shape Space. Graphical shape data is often high dimensional and complex, requiring tools for dimension reduction for analysis and modeling. In past shape analysis, the tangent PCA has been used to perform dimension reduction and discover dominant modes of variability in the shape data. Given the graph shape metric d_g and the definition of shape mean A_μ , we can extend TPCA to graphical shapes in a straightforward manner. As mentioned earlier, due to the non-registration of nodes in the raw data, the application of TPCA directly in $\mathcal A$ will not be appropriate. Instead, one can apply TPCA in the quotient space $\mathcal G$, as described in Algorithm 3. After TPCA, one can represent the graphs using low-dimensional Euclidean coefficients, which facilitates further statistical analysis. Besides TPCA, one may pursue geodesic PCA to reduce dimensions [Bigot et al. (2017); Calissano, Feragen and Vantini (2020); Cazelles et al. (2018); Huckemann, Hotz and Munk (2010)] —implementation of geodesic PCA for elastic graphs will be a direction of future research.

Algorithm 3 Graph TPCA in \mathcal{G}

Given adjacency matrices A_i , i = 1, ..., m:

- 1: Find the mean A_{μ} using Algorithm 1 or 2. They results in the mean and the registered graphs $A_i^*, i = 1, 2, ..., m$.
- 2: For each i, evaluate the shooting vectors $v_i = (A_i^* A_\mu)$ as elements of $T_{A_\mu}(\mathcal{G})$ (the tangent space of \mathcal{G} at A_μ).
- 3: Perform PCA using the shooting vectors $\{v_i, i=1,2,\ldots,m\}$ in $T_{A_{\mu}}(\mathcal{G})$. Obtain principal directions and singular values for the principal components.

Bottom of Fig. 5 shows an example of this TPCA procedure for graphical shapes. The figure shows shape variability along the first two principal directions. As we can see, the first principal direction mainly changes the smaller edges' shapes since the largest path is essentially the same across all the graphs.

4. Brain Artery Networks. Having developed tools for registering, comparing, and summarizing graphs using means and covariance, we now turn our attention to BAN data analysis [Bullitt et al. (2005)].

We study the data from a geometric point of view and analyze these brain networks' shapes. From an anatomical perspective, it seems natural to divide the full network into four components, as shown in Fig. 1. This division helps us focus on comparing individual components across subjects and makes the computational tasks more efficient. The original data has 98 subjects, but we remove six that are difficult to separate into components, resulting in a sample size of N=92. In the supplementary material [Guo et al. (2021)], we provide some relevant statistics on the numbers of nodes and edges in the four components over the selected sample. As these histograms show, these graphs differ significantly in the numbers of nodes and edges across subjects. Additionally, there are large differences in both the shapes and the patterns of arteries forming these networks. Consequently, analyzing the shapes of these BANs is quite challenging and remains relatively unexplored in the past.

- 4.1. Geodesic Deformations. We use the techniques developed in this paper to compute geodesic paths between BAN components and present some examples in Fig. 6. We use both the edge and node attributes in these experiments, with λ selected manually through trial and error. The first column in each row shows a geodesic comparing a BAN component of one subject to that of another, as elements of \mathcal{G} . To improve visual clarity, we remove some unmatched edges from the graphs and plot the same geodesic again in the right column. We have used color-coding of edges to show registration and to track the deformation of each edge. These geodesics are useful in several ways. They provide registrations of arteries across networks, and they help follow deformations of matched arteries from one network to another.
- 4.2. Average BAN Shapes. For the given 92 BANs, it is informative to compute their mean shape. Since the computational cost of pairwise matching of graphs is high, the computation of mean graph using Algorithm 1 becomes very expensive. To accelerate this process, we approximated the mean algorithm by registering each graph to the largest size graph in the dataset. We then used the fixed registration to compute the mean. This registration is not optimal, but it represents a tradeoff between accuracy and computational cost. In order to quantify this approximation, we perform a simple experiment. We take a small set of BANs, say 8 graphs, and compute three different pairwise distance matrices for them: (1) the distance d_b without any registration, (2) the distance \tilde{d}_b , which is pairwise d_b after registering all

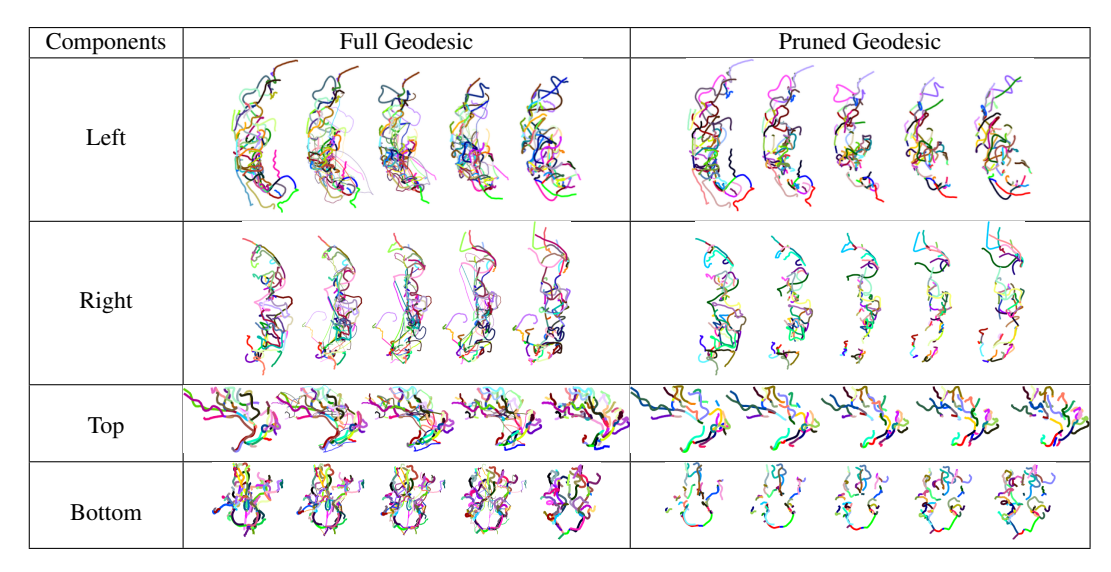


FIG 6. Geodesics between BAN components. In each row we first show the full geodesic and then show a pruned geodesic where the unmatched edges are dropped.(GIF animations of these geodesics are provided with the supplementary material [Guo et al. (2021)].)

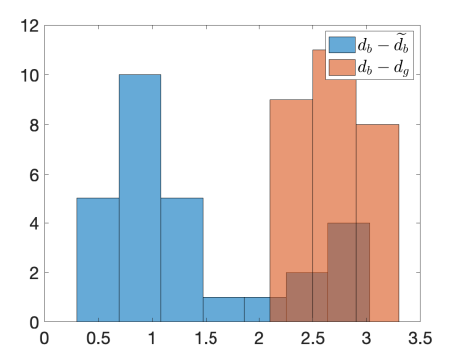


FIG 7. Histograms of decreases in distances due to: (1) pairwise registration (red) and (2) registered to the largest graph (blue).

of them to the largest BAN in the group, and (3) the distance d_g after optimal pairwise registration. Fig. 7 shows the results using histograms of two quantities: (1) $d_b - \tilde{d}_b$ in blue, and (2) $d_b - d_g$ in red. This plot underscores that the proposed approximation provides reasonable gains in distance computations at very small computational cost. Here we have tried one solution, i.e., matching all the graphs to the largest graph, but there are other choices too, each representing its own tradeoff. For instance, one can cluster the graphs into smaller groups and then iteratively improve the registration between and across the clusters. Another idea is to train graph neural networks for performing graph matching. In case there is sufficient training data available, neural networks can provide very efficient computational solutions. Of course, any such solution can be good or bad depending upon actual structural variability in the data. One can always return to the pairwise optimal matching if accuracy is the real concern and the computational cost is less relevant.

Figure 8 shows the resulting mean shapes for each of the four components across 92 subjects. Since these 92 graphs differ in the number, connectivities, and shapes of edges, it is not easy to visualize and interpret the mean shapes. One needs to view 3D displays of

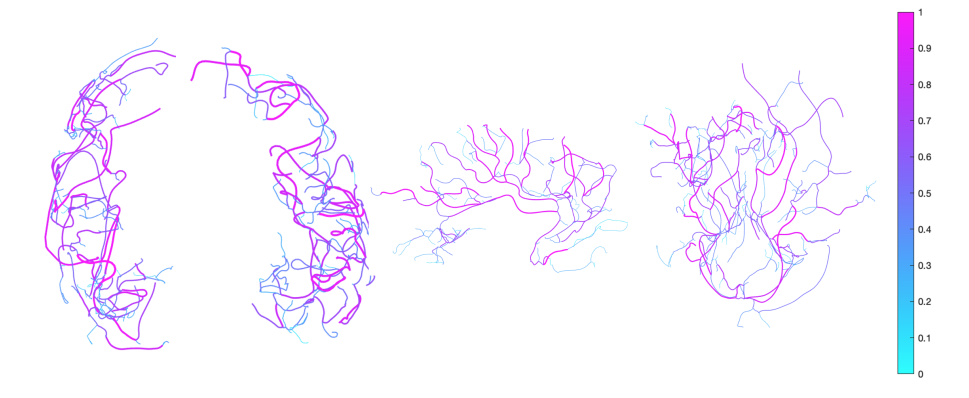


FIG 8. Average shapes of BAN components across 92 subjects. From left to right, it is the mean shape for left, right, top, and bottom components, respectively. The color and thickness of an edge represents its proportional presence in individual subjects – a more red and thicker edge indicates it is present in more subjects.

these shapes to appreciate how well these means capture the common structures in individual graphs. We use the color and thickness of edges to denote the proportion of individual graphs in which that particular edge is present. As expected, these mean shapes show a smoother, broader representation of individual shapes and mainly preserve connectivity patterns present in the data.

The computation of an average shape is a significant, novel result and has not been achieved previously for BANs or any similar graph data. Its importance lies in our need to separate structures common to all subjects from structures that distinguish subjects from each other. By separating this variability, one can focus on individual differences and model this variability using statistical models. Once the common structures have been removed, the subsequent statistical analysis simplifies greatly. We present these studies in the next few sections.

4.3. PCA-Based Analysis of Covariate Effects on Shape. An essential use of the proposed framework is in understanding the effects of covariates, such as gender and age, on shapes of BANs. Due to the high dimensionality and complex nature of BANs, this task is nearly impossible in its original space. We use the elastic shape analysis framework to compute average shapes, extract individual variability, and focus on modeling this individual variability against covariates. As earlier, we do this component-wise, *i.e.*, a separate analysis of each component of BAN.

We first perform Graph PCA using Algorithm 3 on BAN components and represent each subject data into a low-dimensional vector space via projection. A BAN component with 197 nodes and 50 sample points along each edge has a discrete representation with $3\times50\times197\times197=5821350$ elements. However, using Graph PCA, we can retain 80% of the variability in the original data using only 60 principal components. To avoid the confounding effect of artery size, we rescale edges by the total artery length for each graph. As a result, we can focus on gender and age effects on the shapes of BANs.

4.3.1. Gender Effect on BAN Shapes. To study the effect of gender on the arterial graph shapes, we implement a two-sample t-test on the first principal scores and a Hotelling's T-squared test on the first few principal scores. The resulting p-values can be found in Table 1. Most of the p-values are high; thus, we do not find any significant difference between the BAN shapes and the gender. To further investigate this result, we also applied a permutation

TABLE 1
Testing of gender effect on principal scores of shapes of brain arterial networks.

	t test	Hotelling's T-squared test				
	PC-1	PC 1-2	PC 1-3	PC 1-4	PC 1-5	
Left	0.1354	0.5228	0.4333	0.5074	0.4009	
Right	0.8868	0.0785	0.1630	0.0792	0.1210	
Top	0.9236	0.6788	0.0676	0.1200	0.1400	
Bottom	0.4005	0.0599	0.1256	0.1447	0.2328	

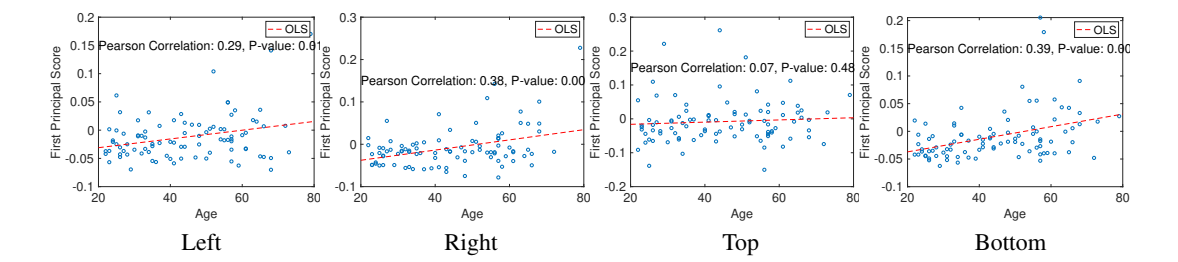


FIG 9. Correlation between the age and the first principal score of shape of arterial networks. To better show the correlation patterns, we removed the maximum principal score for those four components, respectively. In addition, we also removed the second maximum for the left component.

test (described in the following paragraphs) and obtained similar results; see Table 2. We note that Bendich et al. (2016) and Shen et al. (2014) reported multiple insignificant and significant p-values on the same data using very different mathematical representations from ours. Whether there is an anatomical shape difference between BANs of female and male subjects remains an open question and requires further investigation.

4.3.2. Age Effects on BAN Shapes. To study the effect of age of a subject on his/her BAN shape, we studied correlations between the age and the PCA scores of arterial shapes. The results are shown in Fig. 9. We found a significant linear correlation between age and first principal scores of brain arteries in most cases (in all except the top component). The correlation coefficients between the first principal shape score for the left, right, and bottom components and age are 0.29, 0.38, and 0.39, respectively. All of them are statistically significant, with corresponding *p*-values being very close to zero. This result is similar to some published results in the literature but obtained using different mathematical representations than ours [Bendich et al. (2016); Shen et al. (2014)]. The strength of our approach lies in our ability to visualize the nature of deformations resulting from aging. As mentioned before, we also use a permutation test to validate the age effects.

Next, we pose an important question: How do the BAN shapes change as a subject gets older? The tools developed in this paper can be used to visualize the effects of aging on the shape of brain arteries, while feature-based methods proposed in the past cannot address this question. Using Algorithm 3, we compute PCA scores for each BAN shape. Treating these scores as a response and age as a predictor, we fit a zero-mean regression model to the data. Note that since principal scores can be used to reconstruct original graphs, we have a way of mapping these representations back to graphs and facilitate visualizations. Therefore, we can visualize the effects of aging on the shapes of BANs, as in Fig 10. Here we fit a linear model using age to predict the first principal scores. To focus visualization on where the changes are occurring, we calculate the edgewise shape differences using the mean shape as baseline and use different colors (rather than gray color) to denote edges with large deformations, *i.e.*, deformations that are larger than 50% of the differences.

Age (from 22 to 79 years)

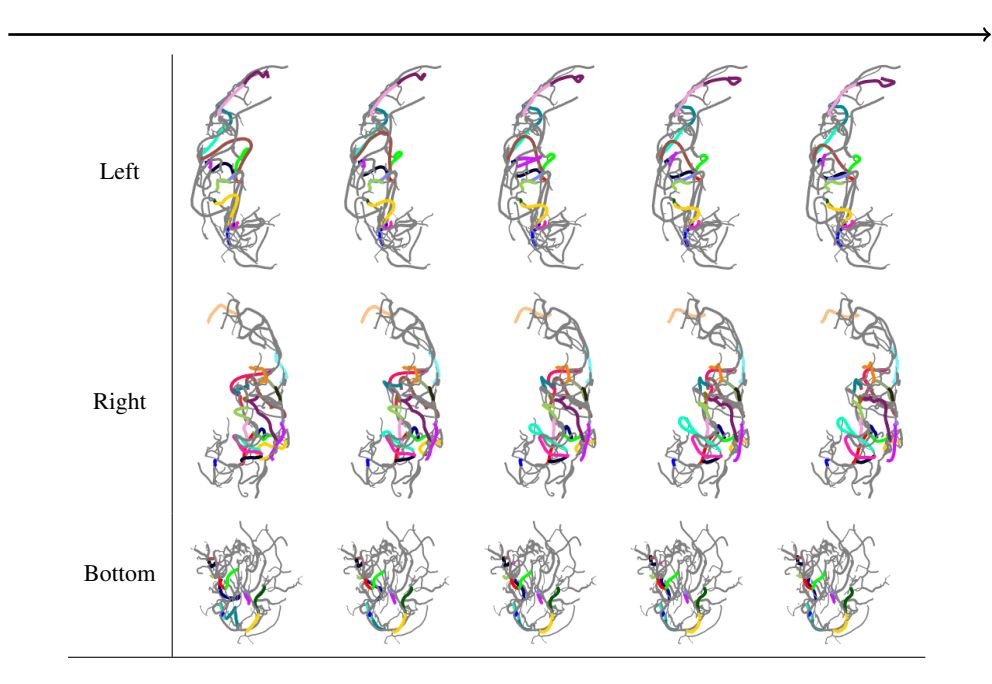


FIG 10. Aging effect on brain arteries. For each component, from left to right is the mean shape deformation when going from age 22 to 79. The colors highlights edges that have large deformations.

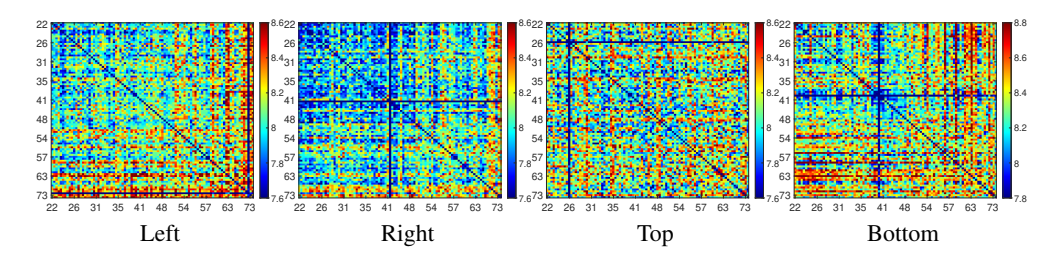


FIG 11. Matrices of shape distances between BAN components of 92 subjects. The axes are labeled by ages.

4.4. Metric-Based Study of Covariates Effects on Shapes. We also investigate the effects of covariates on full BAN shapes using the shape metric d_g (Eqn. 2.2) directly. Fig. 11 shows matrices of pairwise distances between subjects, one matrix for each of the four components separately. (As mentioned before, we have scaled the edges by the total artery length; thus, the distances quantify only shape differences.) We reorder the distance matrices by the age of subjects to help elucidate the effect of aging on shape variability. The color pattern of pixels in these matrices shows that shape distances increase with age (darker red colors are towards the bottom right). This pattern implies that brain arterial networks' shape variability grows with age for three of the four components. This pattern does not seem to hold for the top component.

To further validate the gender and age effects, we implement a permutation test [Hagwood et al. (2013)] based on shape metric d_g . The basic idea is as follows. We divide the subjects into two groups – older than 50 and younger than 50 – and compute a two-sample shape test statistic specified in [Hagwood et al. (2013)]. For two groups, labeled A and B, the test

TABLE 2
Permutation test of gender and age effect on distances of shapes of brain arterial networks.

	Left	Right	Тор	Bottom
Gender	0.0385	0.2128	0.4835	0.0706
Age	0.0006	0	0.4772	0

statistics is defined to be:

$$\left(\frac{2}{m_1 m_2} \sum_{a_i \in A} \sum_{b_j \in B} d_g(g_{a_i}, g_{b_j}) - \frac{1}{m_1^2} \sum_{a_i \in A} \sum_{a_j \in A} d_g(g_{a_i}, g_{a_j}) - \frac{1}{m_2^2} \sum_{b_i \in B} \sum_{b_j \in B} d_g(g_{b_i}, g_{b_j})\right).$$

Here m_1 and m_2 are the sizes of the two sets A and B, respectively. We evaluate the significance of this value using a Permutation test.

That is, we repeat this process 30K times, each time randomly assigning subjects into different groups and computing the test statistics. Using a histogram of the 30K test statistics, we can compute the p-value of the real-data test statistic. The result can be found in Table 2. While the gender effect remains unclear, one can see a significant age effect on the brain arteries for the left, right, and bottom components. We also see that the top component remains relatively unchanged between young and older people. (We remind the reader that the pairwise distance used here is an approximation because of the considerable computational cost associated with the exact computation. Here we first match each graph to the largest graph in the dataset and compute pairwise shape distances between them without any further matching.)

5. Improving Registration Using Landmarks. As stated earlier, matching parts of BANs is the most crucial bottleneck in the shape analysis of elastic graphs. The procedure laid out so far for graph matching is fully automated but, in the end, does not guarantee a global solution. One can potentially improve this solution in case there is some extra matching information. This knowledge can be in the form of some prominent points, called *landmarks*, that have known registrations across graphs. In this context, two issues arise: (1) How can we obtain the landmarks? and (2) How to incorporate this extra information in improving dense registration of graphs?

For the first issue, there are several possibilities. The landmarks may be provided by the domain experts using manual analysis. Another possibility is to perform a preliminary investigation of the data and extract some landmarks of interest. To facilitate this approach, one can use traditional graph-theoretic tools to discover and extract some prominent landmarks automatically. Examples of relevant tools include multi-resolution representations of graphs, clustering of nodes using graph spectra, and Dijkstra's method for finding the longest paths in a graph. For instance, one can use the longest arteries in BANs, extract some prominent nodes lying on them, and use them as landmarks for matching across BANs.

The second issue – how to incorporate given landmarks registration in solving Eqn. 2.2 – is more methodological. We will assume that all landmarks are *nodes* in the original graphs, although one can relax this assumption albeit at the cost of some increased computational complexity. For these *registered nodes*, the corresponding entries of $P \in \mathcal{P}$ are fixed and no longer part of the search. Assuming $n_0 \le n$ to be the number of landmarks, the search space is now reduced to $(n - n_0) \times (n - n_0)$ permutation matrices. This constrained search has also been called *seeded graph matching* in the literature [Fishkind et al. (2012)].

We present an example of landmark-driven matching in Fig. 12. In this example, we study two BANs shown in the two left and the right corners of the top row. We use five landmarks – one at a central node and two each placed automatically along the two longest paths in the graph starting from the central node – to perform improved registration of the graphs.

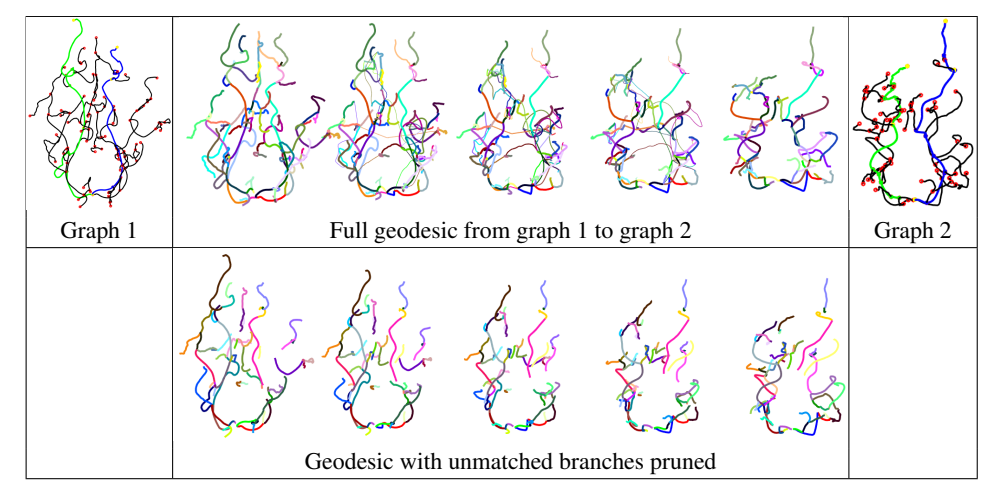


FIG 12. Geodesic path between two BANs (bottom components) using five registered landmarks.

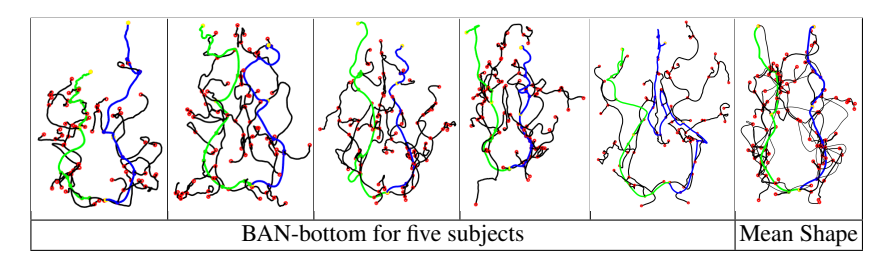


FIG 13. Sample mean of BAN components using improved landmark-based registration.

The resulting geodesic is presented in the top row. We prune this display by removing the unmatched edges and show the pruned geodesic in the bottom row. In this example, the geodesic distance before using landmarks is 244.1698 but comes down to 237.3467 after using landmarks, signifying an improvement in the registration of nodes. We demonstrate an example of landmark-based matching and mean computation in Fig. 13. The use of landmarks improves the registration and thus keeps the major patterns (two longest paths) for the mean.

6. Conclusion. This paper develops techniques for mathematically representing and statistically analyzing shapes of Brain Arterial Networks or BANs, broken into four major components. These objects – BAN components – are complicated due to arbitrary numbers, shapes, sizes, and connectivities of 3D arterial curves. We represent them using elastic graphs and their adjacency matrices, where entries in adjacency matrices are the shapes of the corresponding edges (arteries). We solve for registration of nodes across graphs between compared and use the shape space's geometry to compute geodesics, sample means, and PCA components of BANs. The sample means help capture prominent common characteristics of different BANs while covariance-PCA analysis helps represent individual variability in a tractable fashion.

The subsequent data analysis shows that age has a significant effect on three components of BANs – left, right, and bottom – but does not affect the top component. We use the tools developed here to visualize the nature of BAN shape variability resulting from aging. Visualizing shapes along the principal directions or age-regression directions is an essential accomplishment of this framework. One can pinpoint arteries that undergo significant deformations and arteries that do not change much over time.

The overall performance of this framework relies on the quality of registration of nodes across graphs. We have shown using landmarks could potentially improve the registration quality. For a discussion on the current computation framework, we refer readers to the supplementary materials [Guo et al. (2021)].

Funding. This research was supported in part by the grants NIH R01 MH120299, NSF DMS 1621787, and NSF DMS 1953087.

SUPPLEMENTARY MATERIAL

Supplement to "Statistical shape analysis of brain arterial networks (BAN)"

Discussion on Computational Issues and Descriptive Statistics of BAN; GIFs of Fig 4 and Fig 6.

REFERENCES

- AYDIN, B., PATAKI, G., WANG, H., BULLITT, E., MARRON, J. S. et al. (2009). A principal component analysis for trees. *The Annals of Applied Statistics* **3** 1597–1615.
- AYLWARD, S. R. and BULLITT, E. (2002). Initialization, noise, singularities, and scale in height ridge traversal for tubular object centerline extraction. *IEEE transactions on medical imaging* **21** 61–75.
- BENDICH, P., MARRON, J. S., MILLER, E., PIELOCH, A. and SKWERER, S. (2016). Persistent homology analysis of brain artery trees. *The annals of applied statistics* **10** 198.
- BIGOT, J., GOUET, R., KLEIN, T. and LÓPEZ, A. (2017). Geodesic PCA in the Wasserstein space by convex PCA. In *Annales de l'Institut Henri Poincaré*, *Probabilités et Statistiques* **53** 1–26. Institut Henri Poincaré.
- BULLITT, E., ZENG, D., GERIG, G., AYLWARD, S., JOSHI, S., SMITH, J. K., LIN, W. and EWEND, M. G. (2005). Vessel tortuosity and brain tumor malignancy: a blinded study1. *Academic radiology* **12** 1232–1240.
- BULLITT, E., ZENG, D., MORTAMET, B., GHOSH, A., AYLWARD, S. R., LIN, W., MARKS, B. L. and SMITH, K. (2010). The effects of healthy aging on intracerebral blood vessels visualized by magnetic resonance angiography. *Neurobiology of aging* **31** 290–300.
- CAELLI, T. and KOSINOV, S. (2004). An eigenspace projection clustering method for inexact graph matching. IEEE transactions on pattern analysis and machine intelligence 26 515–519.
- CALISSANO, A., FERAGEN, A. and VANTINI, S. (2020). Populations of Unlabeled Networks: Graph Space Geometry and Geodesic Principal Components.
- CAZELLES, E., SEGUY, V., BIGOT, J., CUTURI, M. and PAPADAKIS, N. (2018). Geodesic PCA versus log-PCA of histograms in the Wasserstein space. *SIAM Journal on Scientific Computing* **40** B429–B456.
- CHAKRABORTY, R. and VEMURI, B. C. (2019). Statistics on the Stiefel manifold: Theory and applications. *Ann. Statist.* 47 415 438.
- CHOWDHURY, S. and NEEDHAM, T. (2020). Gromov-Wasserstein Averaging in a Riemannian Framework. In *The IEEE/CVF Conference on Computer Vision and Pattern Recognition (CVPR) Workshops.*
- COUR, T., SRINIVASAN, P. and SHI, J. (2007). Balanced graph matching. In *Advances in Neural Information Processing Systems* 313–320.
- DRYDEN, I. L. and MARDIA, K. V. (2016). Statistical shape analysis: with applications in R 995. John Wiley & Sons.
- DUNCAN, A., KLASSEN, E., SRIVASTAVA, A. et al. (2018). Statistical shape analysis of simplified neuronal trees. *The Annals of Applied Statistics* **12** 1385–1421.
- FISHKIND, D. E., ADALI, S., PATSOLIC, H. G., MENG, L., SINGH, D., LYZINSKI, V. and PRIEBE, C. E. (2012). Seeded graph matching. *arXiv* preprint arXiv:1209.0367.
- GOLD, S. and RANGARAJAN, A. (1996). A graduated assignment algorithm for graph matching. *IEEE Transactions on pattern analysis and machine intelligence* **18** 377–388.
- GUO, X., SRIVASTAVA, A. and SARKAR, S. (2021). A Quotient Space Formulation for Generative Statistical Analysis of Graphical Data. *Journal of Mathematical Imaging and Vision* 1–18.
- GUO, X., BASU BAL, A., NEEDHAM, T. and SRIVASTAVA, A. (2021). Supplement to "Statistical shape analysis of brain arterial networks (BAN)".
- HAGWOOD, C., BERNAL, J., HALTER, M., ELLIOTT, J. and BRENNAN, T. (2013). Testing Equality of Cell Populations Based on Shape and Geodesic Distances. *IEEE Transactions on Medical Imaging* 32.
- HOOVER, A., KOUZNETSOVA, V. and GOLDBAUM, M. (2000). Locating blood vessels in retinal images by piecewise threshold probing of a matched filter response. *IEEE Transactions on Medical imaging* **19** 203–210.

- HUCKEMANN, S., HOTZ, T. and MUNK, A. (2010). Intrinsic shape analysis: Geodesic PCA for Riemannian manifolds modulo isometric Lie group actions. *Statistica Sinica* 1–58.
- JAIN, B. J. and OBERMAYER, K. (2009). Structure spaces. Journal of Machine Learning Research 10 2667–2714.
- JAIN, B. J. and OBERMAYER, K. (2011). Graph quantization. Computer Vision and Image Understanding 115 946–961.
- JAIN, B. J. and OBERMAYER, K. (2012). Learning in Riemannian orbifolds. arXiv preprint arXiv:1204.4294.
- JERMYN, I. H., KURTEK, S., KLASSEN, E. and SRIVASTAVA, A. (2012). Elastic shape matching of parameterized surfaces using square root normal fields. In *European conference on computer vision* 804–817. Springer.
- JERMYN, I. H., KURTEK, S., LAGA, H. and SRIVASTAVA, A. (2017). Elastic shape analysis of three-dimensional objects. Synthesis Lectures on Computer Vision 12 1–185.
- KENDALL, D. G. (1984). Shape manifolds, procrustean metrics, and complex projective spaces. *Bulletin of the London mathematical society* **16** 81–121.
- KENDALL, D. G., BARDEN, D., CARNE, T. K. and LE, H. (1999). Shape and shape theory. Wiley.
- KLASSEN, E., SRIVASTAVA, A., MIO, M. and JOSHI, S. H. (2004). Analysis of planar shapes using geodesic paths on shape spaces. *IEEE transactions on pattern analysis and machine intelligence* **26** 372–383.
- KONG, J.-H., FISH, D. R., ROCKHILL, R. L. and MASLAND, R. H. (2005). Diversity of ganglion cells in the mouse retina: unsupervised morphological classification and its limits. *Journal of Comparative Neurology* 489 293–310.
- KOOPMANS, T. C. and BECKMANN, M. (1957). Assignment problems and the location of economic activities. *Econometrica: journal of the Econometric Society* 53–76.
- LAWLER, E. L. (1963). The quadratic assignment problem. *Management science* **9** 586–599.
- LEBRIGANT, A. (2019). A Discrete Framework to Find the Optimal Matching Between Manifold-Valued Curves. **61** 40-70.
- LEORDEANU, M. and HEBERT, M. (2005). A spectral technique for correspondence problems using pairwise constraints. In *Tenth IEEE International Conference on Computer Vision (ICCV'05) Volume 1* **2** 1482–1489. IEEE
- LEORDEANU, M., HEBERT, M. and SUKTHANKAR, R. (2009). An integer projected fixed point method for graph matching and map inference. In *Advances in neural information processing systems* 1114–1122.
- LIU, Z.-Y., QIAO, H. and XU, L. (2012). An extended path following algorithm for graph-matching problem. *IEEE transactions on pattern analysis and machine intelligence* **34** 1451–1456.
- SHEN, D., SHEN, H., BHAMIDI, S., MUÑOZ MALDONADO, Y., KIM, Y. and MARRON, J. S. (2014). Functional data analysis of tree data objects. *Journal of Computational and Graphical Statistics* 23 418–438.
- SMALL, C. G. (1996). The Statistical Theory of Shape. Springer.
- SONNENSCHEIN, A., VANDERZEE, D., PITCHERS, W. R., CHARI, S. and DWORKIN, I. (2015). An image database of Drosophila melanogaster wings for phenomic and biometric analysis. *GigaScience* 4 25.
- SRIVASTAVA, A. and KLASSEN, E. P. (2016). Functional and shape data analysis. Springer.
- SRIVASTAVA, A., KLASSEN, E., JOSHI, S. H. and JERMYN, I. H. (2011). Shape analysis of elastic curves in euclidean spaces. *IEEE Transactions on Pattern Analysis and Machine Intelligence* 33 1415–1428.
- UMEYAMA, S. (1988). An eigendecomposition approach to weighted graph matching problems. *IEEE transactions on pattern analysis and machine intelligence* **10** 695–703.
- VOGELSTEIN, J. T., CONROY, J. M., LYZINSKI, V., PODRAZIK, L. J., KRATZER, S. G., HARLEY, E. T., FISHKIND, D. E., VOGELSTEIN, R. J. and PRIEBE, C. E. (2015). Fast approximate quadratic programming for graph matching. *PLOS one* **10** e0121002.
- WANG, G., LAGA, H., JIA, J., MIKLAVCIC, S. J. and SRIVASTAVA, A. (2020). Statistical analysis and modeling of the geometry and topology of plant roots. *Journal of Theoretical Biology* **486** 110108.
- WASSERMAN, L. (2018). Topological data analysis. Annual Review of Statistics and Its Application 5 501–532.
- YAN, J., YIN, X.-C., LIN, W., DENG, C., ZHA, H. and YANG, X. (2016). A short survey of recent advances in graph matching. In *Proceedings of the 2016 ACM on International Conference on Multimedia Retrieval* 167–174.
- YOUNES, L. (1998). Computable elastic distance between shapes. SIAM Journal of Applied Mathematics 58 565-586.
- YOUNES, L., MICHOR, P. W., SHAH, J., MUMFORD, D. and LINCEI, R. (2008). A Metric on Shape Space with Explicit Geodesics. *Matematica E Applicazioni* 19 25–57.
- ZANFIR, A. and SMINCHISESCU, C. (2018). Deep learning of graph matching. In *Proceedings of the IEEE Conference on Computer Vision and Pattern Recognition* 2684–2693.
- ZHANG, Z., KLASSEN, E. and SRIVASTAVA, A. (2018). Phase-amplitude separation and modeling of spherical trajectories. *Journal of Computational and Graphical Statistics* 27 85–97.
- ZHOU, F. and DE LA TORRE, F. (2012). Factorized graph matching. In 2012 IEEE Conference on Computer Vision and Pattern Recognition 127–134. IEEE.

ZHOU, F. and DE LA TORRE, F. (2015). Factorized graph matching. *IEEE transactions on pattern analysis and machine intelligence* **38** 1774–1789.